Temperature-independent emission in a $[(CH_3)NPh]_2MnBr_4$ single crystal analogous to thermally activated delayed fluorescence

Mutibah Alanazi[1], Atanu Jana[2], Won Woong Choi[3,4], Robert A. Taylor[1], Chang Woo Myung[3,4], Youngsin Park[5]

[1]Clarendon Laboratory, Department of Physics, University of Oxford, Parks Road, Oxford OX1 3PU, UK

[2]Division of Physics and Semiconductor, Dongguk University, Seoul 04620, Korea

[3]Department of Energy Science, Sungkyunkwan University, Suwon 16419, Korea

[4]Center for 2D Quantum Heterostructures, Institute for Basic Science (IBS), Suwon 16419, Korea

[5]Department of Chemistry, College of Natural Science, Ulsan National Institute of Science and Technology, Ulsan 44919, Korea

We demonstrate a novel thermally activated delayed fluorescence-like mechanism in $[(CH_3)NPh]_2MnBr_4$ single crystals, driven by the coexistence of temperature-sensitive shallow traps and temperature-independent deep traps introduced by Br vacancies. Through comprehensive temperature-dependent photoluminescence (PL) and time-resolved PL measurements, combined with first-principles calculations, we reveal that the material exhibits exceptional thermal stability, retaining 67% of its relative PL quantum yield at room temperature and achieving an absolute quantum yield of ~38.9% under optimal excitation conditions. The dual-component PL decay dynamics consist of a fast decay (~hundreds of ps) governed by shallow traps and a long decay (~350 μs) dominated by deep traps, creating an energy cascade that efficiently promotes radiative recombination while minimizing non-radiative losses. Our findings provide critical insights into defect-mediated luminescence mechanisms and establish $[(CH_3)NPh]_2MnBr_4$ as a lead-free, thermally stable material with high efficiency, making it an excellent candidate for next-generation optoelectronic applications, including solid-state lighting and temperature-sensitive devices.

Introduction

Hybrid organic-inorganic perovskites have transformed optoelectronic research due to their exceptional optical and electronic properties, including tunable bandgaps, high photoluminescence quantum yields (PLQY), and solution processability.[1,2,3,4,5] Despite these advantages, their widespread adoption has been limited by the use of toxic lead and inherent stability issues, driving the search for lead-free alternatives that offer comparable or superior performance. Among emerging candidates, $[(CH_3)NPh]_2MnBr_4$ single crystals (SCs) exhibit promising properties, combining strong thermal stability with high PLQY. Unlike conventional lead-free perovskites, such as $Cs_2AgBiBr_6$ and $Cs_2InAgCl_6$, which typically show single-component emission, low PLQY (<20%), and significant thermal quenching,[6,7] $[(CH_3)NPh]_2MnBr_4$ stands out for its dual-component PL decay dynamics and superior quantum efficiency. Despite these promising characteristics, the microscopic origins of its luminescent behavior—particularly the role of defect states—remain poorly understood. Thermally activated delayed fluorescence (TADF) has been extensively studied in organic systems as a mechanism for achieving high luminescence efficiency by harvesting both singlet and triplet excitons through reversible intersystem crossing.[8,9,10] Although TADF-like behavior has been observed in some perovskite materials,[11,12] the underlying luminescence mechanisms in hybrid perovskites remain largely unexplored. Here, we report a novel defect-engineered luminescence mechanism in $[(CH_3)NPh]_2MnBr_4$, combining temperature-dependent optical spectroscopy and first-principles calculations. The material maintains 67% of its relative PLQY at room temperature (RT) compared to low temperatures and demonstrates an absolute quantum yield (AQY) of 38.9%, as measured using an integrating sphere. This high thermal stability is driven by the interplay between shallow and deep defect states.[13,14] Our analysis identifies two types of defect states introduced by Br vacancies: deep traps that enable temperature-independent, long-lived emission (~350 μs) and shallow traps responsible for

temperature-dependent fast decay (~100 ps). This dual-trap system enhances radiative recombination while minimizing non-radiative losses. These findings highlight $[(CH_3)NPh]_2MnBr_4$ as a lead-free, thermally stable material for next-generation optoelectronic devices, demonstrating the power of defect engineering in hybrid perovskites.[15,16,17]

Results and discussion.

Figures 1a and 1c show the excitation power-dependent PL spectra of $[(CH_3)NPh]_2MnBr_4$ SCs at 5 K and 300 K, respectively. At 5 K, the PL spectra exhibit a Gaussian shape across the entire range of excitation densities, with the peak position remaining stable at 2.35 eV. The PL peak increases linearly with excitation power without significant broadening or shifting of the peak, indicating efficient radiative recombination with minimal non-radiative losses. The stability of the peak position and shape suggests that the material's electronic states are robust and unaffected by excitation power at low temperatures. At 300 K, the PL spectra exhibit a similar linear increase in intensity with excitation power, but with slight broadening of the peak at higher excitation powers. This broadening is likely due to increased phonon interactions and carrier-carrier scattering, which become more prominent at elevated temperatures. Despite this, the peak position remains centered around 2.35 eV, demonstrating the stability of the emission mechanism even at RT. Figures 1b and 1d present the integrated PL intensities (I_{PL}) as a function of excitation power on a log-log scale at 5 K and 300 K, respectively. The data follow a power-law dependence, $I_{PL} \propto (I_{exc})^k$,[18,19] where the extracted k values are 1.05 at 5 K and 1.03 at 300 K. The near-linear relationship ($k \approx 1$) suggests that radiative recombination dominates over non-radiative processes, with minimal contributions from Auger recombination or other non-radiative pathways. However, $k \approx 1$ does not differentiate between excitonic and trap-mediated recombination. At 5 K, the lack of peak broadening and the near-unity k value confirm minimal involvement of non-radiative processes. At 300 K, the slightly reduced k value

and peak broadening suggest the onset of non-radiative recombination pathways, such as phonon-assisted recombination and carrier trapping. These non-radiative processes become more significant at higher temperatures due to thermal activation. The difference in behavior between 5 K and 300 K highlights the role of temperature in activating non-radiative pathways. While phonon interactions and defect-related carrier trapping increase at higher temperatures, the near-linear power dependence of I_{PL} indicates that radiative recombination remains a significant contributor to the overall PL efficiency.

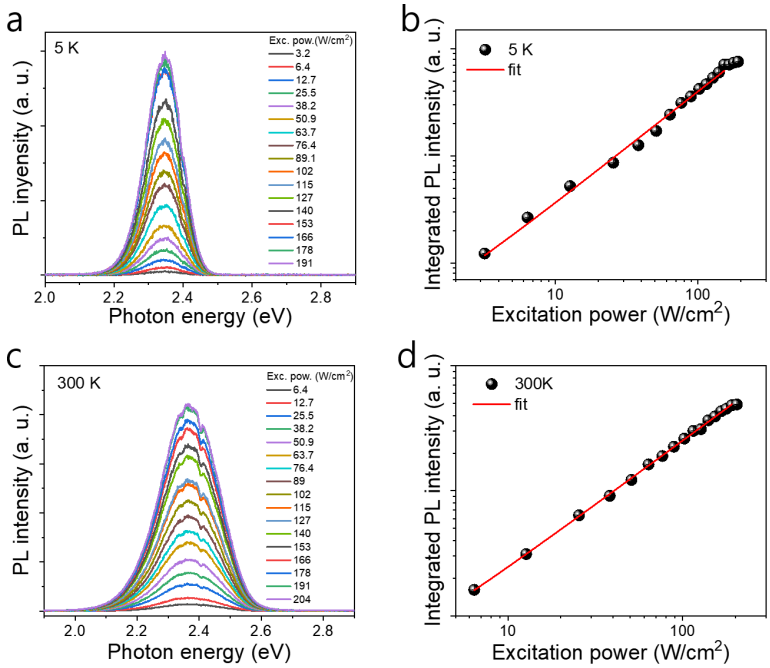

Fig. 1. **Excitation power dependent PL**. Excitation power dependent PL spectra of the $[(CH_3)NPh]_2MnBr_4$ single crystal measured at 5 K with excitation powers ranging from 3.2 W/cm² to 191 W/cm² (a). and 300 K with excitation powers ranging from 6.4 W/cm² to 204 W/cm² (c). The integrated PL intensity as a function of excitation density at 5 K (b) and 300 K (d). The red solid lines are fitted results.

Figure 2a shows the PL spectra of $[(CH_3)NPh]_2MnBr_4$ SCs measured at various temperatures under an excitation power density of 6.4 W/cm² to minimize thermal effects. At 10 K, the PL spectrum exhibits a sharp, intense peak centered around 2.35 eV, reflecting high radiative recombination efficiency. As the temperature increases, the PL peak rapidly decreases up to 50

K, followed by a gradual decline accompanied by peak broadening. A blueshift in the PL peak energy with increasing temperature is observed, consistent with behavior in hybrid perovskites, which is attributed to lattice expansion, dynamic disorder, and electron-phonon interactions.[15,17,20] Figure 2b provides normalized PL spectra as a function of temperature, along with a color map showing the temperature-dependent spectral evolution. The emission energy undergoes an initial redshift below 50 K, followed by a significant blueshift as the temperature increases further, indicating complex temperature-dependent processes. The "kink" in the PL energy at ~50 K is attributed to a phase transition, a feature commonly observed in hybrid perovskites. The integrated PL intensity (I_{PL}) (Fig. 2c) shows a sharp decline up to 50 K, after which it remains nearly constant at higher temperatures. The initial rapid drop in I_{PL} is attributed to the activation of non-radiative recombination pathways, such as thermally activated traps and phonon interactions, which become more prominent as the temperature increases. Above 50 K, the nearly constant I_{PL} suggests that radiative and non-radiative recombination processes reach a steady balance, with minimal further activation of non-radiative pathways at elevated temperatures. The sharp decrease in I_{PL} up to 50 K can be attributed to changes in excitonic processes, such as exciton formation, diffusion, and recombination, which are strongly influenced by thermal variations. Additionally, energy transfer mechanisms between the organic and inorganic components of the crystal lattice may be affected by temperature,[21,22,23,24] leading to modulation of luminescent behavior. The structural stability of the crystal plays a key role in maintaining consistent luminescence intensity up to 300 K, with minimal variation observed compared to typical semiconductors. In most semiconductors, the I_{PL} typically decreases by two to three orders of magnitude as the temperature rises to 300 K, due to thermal quenching caused by carrier trapping at surface states or thermal escape via longitudinal optical (LO) phonon scattering.[25] However, $[(CH_3)NPh]_2MnBr_4$ exhibits exceptional thermal stability, with its I_{PL} at 300 K decreasing by

only 1.5 times compared to that at 10 K. This performance is a significant improvement over many other luminescent materials, which experience severe I_{PL} drops at RT, often resulting in a PLQY of ~1%.[26,27] Assuming minimal non-radiative recombination at 10 K, the PLQY at 300 K is estimated to be ~67% by normalizing the I_{PL} at 10 K to 100% and comparing it to the I_{PL} at 300 K under identical conditions. This estimation provides a relative measure of thermal stability rather than an AQY value. The high retention of PLQY underscores the material's robustness against thermal quenching and suggests efficient radiative recombination processes dominate over non-radiative pathways across the studied temperature range. The high PLQY retention at RT highlights the potential of $[(CH_3)NPh]_2MnBr_4$ for practical optoelectronic applications, particularly where both thermal stability and high efficiency are essential. The minimal reduction in PLQY suggests limited activation of non-radiative recombination pathways even at elevated temperatures. While the indirect estimation method does not provide absolute PLQY values, it clearly demonstrates the exceptional temperature stability of the radiative processes. This distinguishes the material from many other luminescent systems and positions it as a strong candidate for high-efficiency light-emitting devices operating at RT. Figure 2d depicts the emission energy as a function of temperature, showing an initial redshift up to 50 K, followed by a blueshift at higher temperatures. This blueshift is linked to electron-phonon coupling, lattice expansion, and dynamic halide-ion disorder, phenomena commonly observed in hybrid perovskites.[17,20,28] In conventional semiconductors, the bandgap typically narrows with temperature, leading to a redshift; however, hybrid perovskites display unique temperature-dependent bandgap behavior due to their soft lattice and dynamic interactions. The full width at half maximum (FWHM: Γ) of the PL peak provides additional insight into temperature-dependent processes. At 10 K, the FWHM is 122 meV, indicating minimal phonon interactions and efficient radiative recombination. As the temperature rises, the FWHM increases linearly to 220 meV at 300 K due to enhanced exciton-phonon interactions. This

broadening can be described by the equation, $\Gamma(T) = \Gamma_0 + \sigma T + \gamma_{LO}/[\exp(-E_{LO}/k_B T) - 1]$,[29,30] where Γ_0 represents the temperature-independent inhomogeneous broadening at 0 K, σ is the coupling coefficient for exciton-acoustic phonon interactions, γ_{LO} is the coupling coefficient for exciton-LO phonon interactions, and E_{LO} is the LO phonon energy. The fitting parameters are σ = 212 μeV/K and γ_{LO} = 57 meV, highlighting strong exciton-phonon coupling at higher temperatures. The decrease in I_{PL} and broadening of the FWHM at higher temperatures point to the activation of non-radiative recombination pathways involving phonons and traps, which compete with radiative processes.

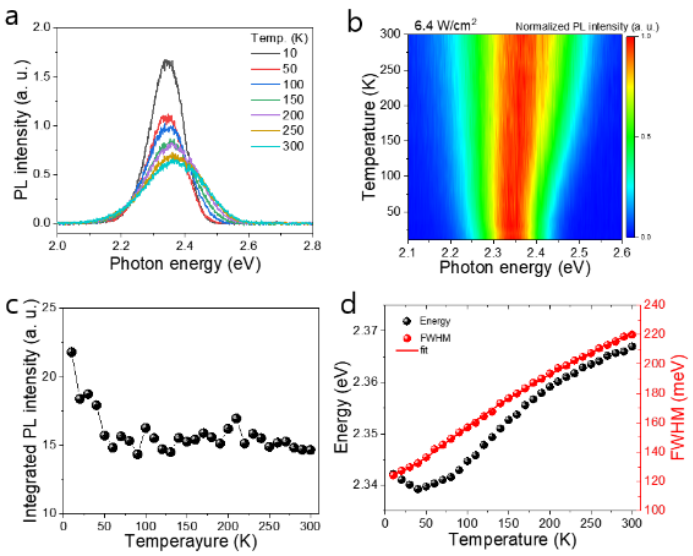

Fig. 2. **Temperature-dependent PL**. (a) Representative PL spectra measured at several temperature of 50 K intervals. (b) Normalized 2-dimensional PL spectra map. (c) Integrated PL intensity as a function of temperature. (d) The PL emission energy and full width at half maximum as a function of temperature.

Figure 3 shows the AQY of $[(CH_3)NPh]_2MnBr_4$ SCs measured at RT using an integrating sphere across an excitation wavelength range of 410–520 nm. Figure 3a presents a 2D contour plot of the PL intensity as a function of excitation and emission wavelengths, revealing a broad emission profile with high PL intensity over a wide range of excitation wavelengths. Figure 3b

displays the AQY, showing a peak value of ~38.9% under excitation between 450 nm and 470 nm. The AQY decreases significantly for excitation wavelengths beyond 500 nm, suggesting less efficient absorption and non-radiative recombination losses at higher wavelengths. This observation highlights that efficient radiative recombination occurs primarily within the optimal excitation range near the material's absorption edge. The maximum AQY near 450–470 nm aligns with the efficient absorption and carrier relaxation near the material's absorption edge. Beyond this range, carriers excited at longer wavelengths encounter less efficient energy transfer to emissive states, leading to reduced AQY. The efficient luminescence within the optimal excitation range is driven by the interplay between shallow and deep defect states. Carriers generated within this range can be efficiently trapped by deep states, promoting stable radiative recombination. The decrease in AQY beyond 500 nm is likely due to the activation of non-radiative pathways, such as phonon scattering and defect-induced recombination losses, which become more prominent outside the optimal excitation range.

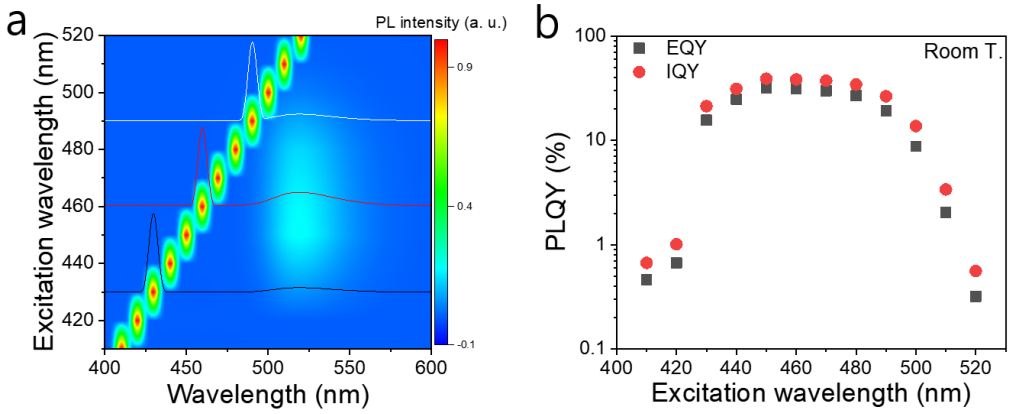

Fig. 3. Absolute quantum yield at RT. (a) 2D contour plot of the PL intensity of $[(CH_3)NPh]_2MnBr_4$ SCs as a function of excitation and emission wavelengths, showing strong PL emission across a wide excitation range (410–520 nm). (b) AQY measured using an integrating sphere, with a peak AQY of ~38.9% observed between 450 nm and 470 nm (Fig. S1.).

The absorption spectrum (Fig. 4a) shows a clear absorption edge at ~2.42 eV, corresponding to the material's bandgap. The PL spectrum features a prominent single emission peak centered around 2.38 eV, with a slight redshift of about 40 meV relative to the absorption edge. This Stokes shift, which arises from the relaxation of photoexcited carriers to lower-energy emissive states before radiative recombination, is relatively small. Such a small Stokes shift indicates efficient radiative recombination with minimal energy loss, reflecting the high crystal quality of the material.[15,17,31] The PL excitation (PLE) spectrum (Fig. 4b) provides further insight into the optical properties. It exhibits a broad excitation band with maximum intensity around 2.35–2.38 eV, consistent with the PL peak observed in Fig. 4a. The PLE intensity gradually increases with higher excitation energies, up to ~2.42 eV, corresponding to the absorption edge. This suggests that higher-energy excitations contribute to the PL emission, likely through rapid carrier relaxation to lower-energy emissive states.[5] The broad width of the excitation band reflects the involvement of multiple electronic states in the absorption and emission processes, which may arise from the complex electronic structure of $[(CH_3)NPh]_2MnBr_4$. The absence of significant PLE intensity at sub-bandgap energies (< 2.3 eV) confirms that excitations below the bandgap are inefficient in generating PL, consistent with the sharp absorption edge observed in the absorption spectrum.

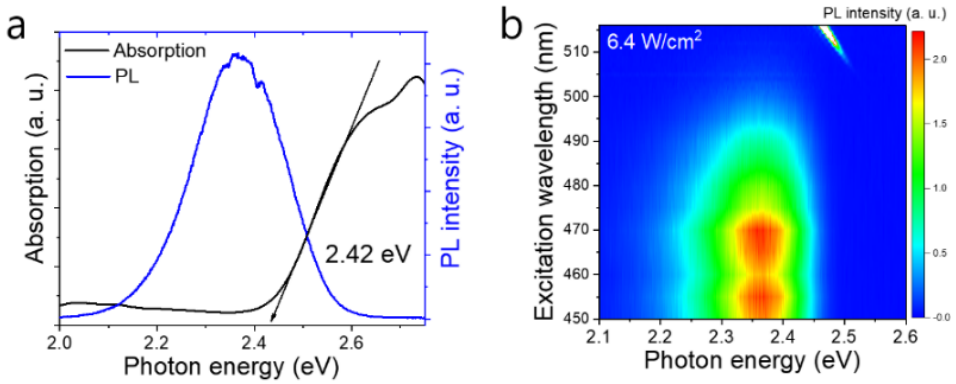

Fig. 4. **Luminescence, absorption, and PLE**. (a) PL and absorption spectra measured at 300 K. (b) PLE spectra measured at 300 K.

Figure 5 illustrates the TRPL decay curves at 300 K, measured across the PL emission. The decay behavior reveals two distinct components: a fast decay with a sub-nanosecond lifetime and a slow decay with a long lifetime of approximately 350 μs. These components represent two different carrier recombination mechanisms governed by defect-mediated processes.[32] The fast decay component is attributed to carrier localization in band tail states near the band edges. The decay times vary with emission energy, as shown in Fig. 5b, indicating that the recombination dynamics are sensitive to the local energy environment. This energy dependence arises because carriers localized in shallow band tail states experience different rates of recombination.[33] The inset of Fig. 5b reveals that the fastest recombination occurs near the PL peak at 2.37 eV, indicating that thermal activation allows carriers to escape shallow traps and recombine radiatively, contributing to the initial rapid PL decay. In contrast, the slow decay component, with a consistent lifetime of approximately 350 μs across the entire PL spectrum (Fig. 5a), is independent of emission energy. This energy independence confirms that the long-lived emission is dominated by deep trap states, which uniformly capture and release carriers over extended timescales, ruling out contributions from band tail states. The coexistence of these two decay components reflects two distinct recombination mechanisms. The fast decay originates from carriers localized in shallow band tail states, where the recombination rate varies with energy due to localization effects. The slow decay, however, is governed by deep traps that act as stable recombination centers, enabling uniform, long-lived emission. This dual-component decay behavior highlights the role of both shallow and deep traps in the complex defect-mediated dynamics of $[(CH_3)NPh]_2MnBr_4$, underscoring their importance in defining its optical properties.

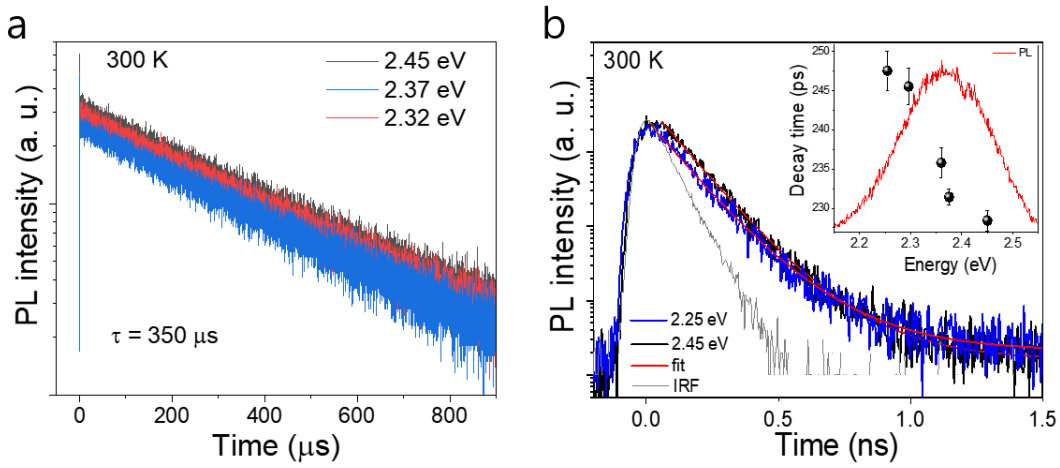

Fig. 5. **TRPL measured at 300 K**. (a) TRPL decay traces of the long-lived component across the PL spectrum using the repetition rate of 80 kHz. The decay time is constant across the PL emission. (b) TRPL decay trace for the short decay component across the PL emission using the repetition rate of 76 MHz. The gray color is IRF and TRPL measurement accuracy is 120 ps. Inset depicts PL spectrum and decay time across the PL.

To elucidate the long-lived decay kinetics, a localization in the band tail states has been proposed.[34] However, the long-lived component exhibited strong temperature dependence, becoming nearly undetectable at temperatures below 150 K. This suggests that the long-lived decay component observed at low temperatures cannot be attributed to detrapping. Nevertheless, the long-lived decay time of the SC remains nearly constant from 5 K to 300 K (Fig. 6a). This suggests a stable concentration of deep defect states that are unaffected by thermal fluctuations. The PL decay profiles at 5 K, 100 K, 200 K, and 300 K demonstrate a consistent long decay component across all temperatures, with the decay time (τ) remaining nearly constant. This temperature-independent decay time suggests that the recombination process is dominated by deep trap states, which uniformly capture and release carriers over extended periods, irrespective of temperature changes. The TRPL decay of trap-related emission exhibits faster thermal quenching of the PL lifetime compared to excitonic emission, allowing us to rule out trap emission.[35] The temperature-independent PL decay time refers to

the duration during which the luminescent intensity remains unaffected by fluctuations in temperature. This phenomenon arises from several key factors: The material may exhibit a stable concentration of defect states across varying temperatures, ensuring stability in the decay time. The mechanisms governing energy transfer within the material, essential for luminescence, may remain unchanged across different temperatures. The structural integrity of the material, including its lattice structure and electronic configuration, may remain intact despite temperature variations. Materials with a uniform composition and minimal phase transitions with temperature are more likely to exhibit temperature-independent decay times, ensuring consistent luminescent behavior across a broad temperature spectrum.

In contrast, Fig. 6b demonstrates a pronounced temperature dependence of the initial fast decay component. As temperature increases from 10 K to 300 K, this rapid decay becomes more prominent and its decay time decreases. Fig. 6c quantifies this trend, showing a clear reduction in the short decay time component with increasing temperature. This behavior is consistent with thermally activated processes involving shallow traps or band tail states. The initial fast decay becomes less pronounced as the temperature decreases. The rapid decay component shows a temperature-dependent behavior, with a decrease in decay time as temperature increases, indicating the involvement of temperature-sensitive processes. The decay time decreases with increasing temperature, suggesting that higher temperatures facilitate faster recombination processes, likely due to increased thermal activation of carriers out of shallow traps or band tail states. The plot of decay time versus temperature shows a nearly constant long decay time component and a short decay time component that decreases with increasing temperature. This behavior can be attributed to different recombination mechanisms dominating at various temperatures. The rapid decay component's temperature dependence can be attributed to factors such as changes in excitonic processes and energy transfer mechanisms influenced by temperature variations. At higher temperatures, carriers are thermally activated

out of shallow states, leading to faster non-radiative recombination processes. The temperature-independent behavior of the slower decay component may arise from stable defect states within the crystal lattice or other intrinsic properties of the material. Deep trap states capture carriers for extended periods, resulting in prolonged emission consistent with deep traps dominating the recombination process regardless of thermal energy. The long decay component is attributed to deep trap states that capture carriers for extended periods. These states are deep enough in the energy landscape that thermal activation has minimal effect on the recombination rate. As a result, the long decay time remains nearly constant across the temperature range. Conversely, the short decay component is influenced by temperature, with the decay time decreasing as temperature increases. This suggests that shallow traps or band tail states contribute significantly to the initial fast recombination. At higher temperatures, carriers are thermally activated out of these shallow states, leading to faster non-radiative recombination processes. This results in a shorter decay time at elevated temperatures. Conversely, at lower temperatures, thermal activation is reduced, allowing carriers to remain trapped in shallow states longer, which leads to a slower initial decay. The behavior of the PL decay times can also be explained in the context of analogous TADF: TADF involves carriers initially trapped in non-radiative states (such as triplet states or shallow traps) that can be thermally activated to radiative states, leading to delayed fluorescence. At higher temperatures, thermal activation is more efficient, enabling carriers to escape from non-radiative states more readily and recombine radiatively, resulting in a shorter decay time. The long decay component remaining nearly constant across different temperatures suggests that deep trap states are not significantly affected by thermal activation. These states capture carriers, leading to prolonged emission. The short decay component's temperature dependence aligns with the TADF mechanism, where shallow trap states or band tail states act as intermediaries. At higher temperatures, carriers are thermally activated out of these shallow states, leading to a faster recombination

process and shorter decay times. It highlights the coexistence of stable deep traps and thermally-sensitive shallow states in $[Me_3NPh]_2MnBr_4$ SCs. The material's ability to maintain consistent long-lived emission across a wide temperature range, combined with tunable fast decay processes, suggests potential applications in temperature-stable optoelectronic devices.

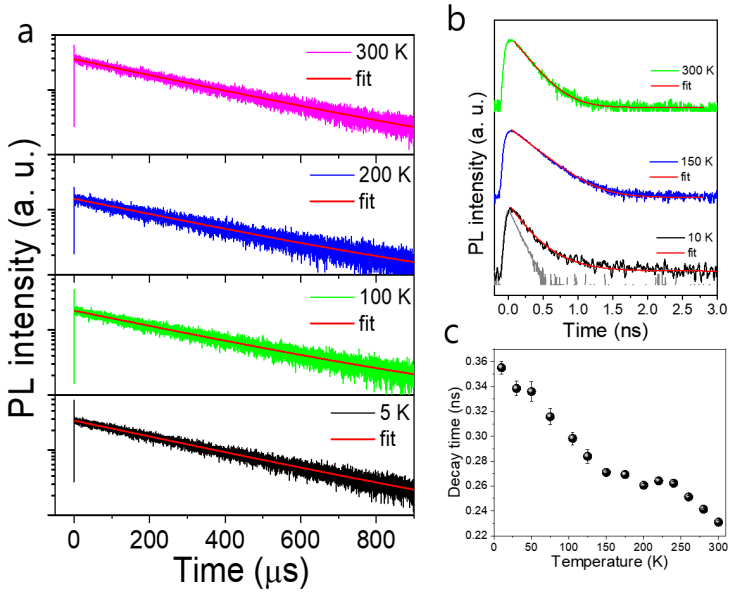

Fig. 6. **Temperature TRPL measurements**. (a) Several temperature-dependent TRPL curves of the SC. The repetition rate of the excitation is 80 kHz. (b) Several temperature-dependent TRPL curves for the fast-lived decay component of the SC. The repetition rate of the excitation is 76 MHz. The gray color presents IRF. (c) Decay time of the fast decay component as a function of temperature.

We used density functional theory (DFT) simulations to investigate the single Br vacancy defect in $[Me_3NPh]_2MnBr_4$ (Fig. 7a).[11] The most stable defect configuration was obtained by removing a single Br atom from the pristine crystal (Fig. S2 and S3). Projected density of states (PDOS) analysis (Fig. 7a) reveals the emergence of several spin-down deep levels and one spin-up shallow level below the conduction band minimum (CBM). These defect states primarily arise from Mn d-orbitals and Br p-orbitals. Among the spin-down trap states, we identified a deep trap (Fig. 7b) at a radiative transition energy of approximately 2.29 eV,

matching the experimentally observed PL emission. The substantial energetic separation of this state ensures stable carrier trapping, which explains the temperature-independent long decay component ($\tau \approx 350$ μs) in TRPL measurements. In addition, the PDOS reveals a spin-up shallow trap located 0.25 eV below the CBM (Fig. 7c). This offset aligns with the thermal activation energy extracted from temperature-dependent TRPL data, clarifying the increased contribution of the fast decay component above 50 K. At these temperatures, carriers would gain sufficient thermal energy to be activated into higher-energy states, accelerating recombination. The shallow trap states are therefore essential to the fast (~100 ps) temperature-dependent decay. Their higher non-radiative recombination rates at elevated temperatures reinforce the rapid decay process, as evidenced by the growing prominence of the fast component above 50 K. Overall, the close agreement between theoretical predictions and experimental observations strongly supports the proposed defect-mediated TADF-like mechanism. The interplay of shallow and deep traps governs the dual-component emission decay, underscoring the critical role of Br-vacancy-induced defect states in defining the optical properties of $[Me_3NPh]_2MnBr_4$ SCs.

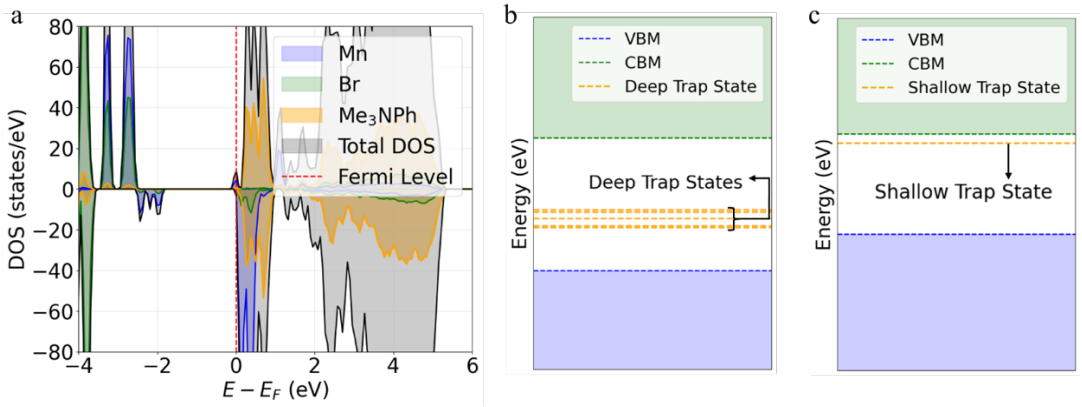

Fig. 7. Density of States. (a) Spin-polarized electronic properties of the defect system, where one Br atom is removed from $[Me_3NPh]_2MnBr_4$. The total and partial density of states of the Br vacancy defect system are shown, with the red dashed line indicating the Fermi energy, which is shifted to zero. Among the spin-down states, (b) deep trap states are identified, and among the spin-up states, (c) shallow trap states are indicated in the Br vacancy defect system.

Conclusions

In conclusion, we have demonstrated a novel defect-mediated luminescence mechanism in $[(CH_3)NPh]_2MnBr_4$ SCs through comprehensive optical measurements and first-principles calculations. Our key findings reveal the following distinctive features. First, the material exhibits exceptional thermal stability, retaining 67% of its relative PLQY at RT and achieving an AQY of ~38.9%. This robust luminescence performance is attributed to the efficient suppression of non-radiative pathways, even at elevated temperatures. Second, we identified two types of defect states, introduced by Br vacancies, through first-principles calculations: temperature-sensitive shallow traps and temperature-independent deep traps. These states play a crucial role in governing the carrier recombination dynamics and luminescent behavior. Third, these coexisting trap states enable a unique TADF-like mechanism, where deep traps provide stable, long-lived radiative channels (~350 μs), while shallow traps facilitate temperature-dependent fast decay (hundreds of ps). The dual-component decay behavior, supported by temperature-dependent TRPL measurements, highlights the role of defect states in modulating radiative and non-radiative recombination processes. This detailed understanding of the interplay between defect states and carrier dynamics not only explains the material's remarkable luminescent properties but also introduces a new design principle for developing high-efficiency light-emitting materials.

Methods

Sample synthesis

$MnBr_2$ and Me_3NPhBr were dissolved in ethanol by sonication. The yellow colored solution was filtered and kept for slow evaporation under ambient conditions. After two weeks, light green crystals were formed. The prepared SC was depicted in supporting information Fig. S4.

XRD measurements

The crystal structure of $[(CH_3)NPh]_2MnBr_4$ was determined by single crystal X-ray diffraction (XRD) using a graphite-monochromated Mo Kα radiation source (λ=0.7107Å). The diffractometer is equipped with a four-circle goniometer, allowing crystal rotation around φ, κ, ω, and 2θ axes. Unit cell parameters were determined by collecting diffracted intensities from 24 frames measured in two different crystallographic zones and analyzed using the method of difference vectors. The crystal structure was solved by direct methods and refined by full-matrix least-squares on F2 using SHELXTL. The XRD result was depicted in supporting information Figure S5 and Figure S6 shows the resulting crystal structure visualization, and Table S1 presents the detailed XRD data including unit cell parameters at different temperatures.

PL measurements

Photoluminescence (PL) measurements were performed using a home-made micro-PL (μPL) setup. The excitation source was a tunable pulsed laser, focused onto the sample using a 100× objective lens, resulting in a spot size of approximately 1 μm^2. The sample was mounted in a continuous-flow helium cryostat, enabling precise temperature control from 5 K to room temperature. For steady-state PL measurements, the emitted luminescence was collected through the same objective lens and directed to a 0.5 m focal length spectrometer equipped

with a 300 grooves/mm grating for spectral analysis. Time-resolved PL (TRPL) experiments were conducted using a 100 fs frequency-doubled Ti:sapphire laser with an excitation wavelength of 395 nm. The laser system was capable of operating at two different repetition rates: 76 MHz for capturing fast decay components, and 80 kHz for slow decay components using a pulse picker system. This dual-rate capability allowed for precise characterization of both rapid and slow decay processes in the PL spectra of $[(CH_3)NPh]_2MnBr_4$ single crystals. The combination of steady-state and time-resolved measurements, along with the wide temperature range, provided comprehensive insights into the photophysical properties and carrier dynamics of the studied material.

PLQY measurements

We measured the absolute quantum yield (AQY) using an FP-8500ST spectrofluorometer equipped with an integrating sphere across an excitation range of 410 nm to 520 nm. $[(CH_3)NPh]_2MnBr_4$ demonstrated a peak AQY of ~38.9% under excitation between 450 nm and 470 nm at room temperature, highlighting efficient radiative recombination within the material. The decrease in AQY beyond this optimal range reflects the activation of non-radiative recombination pathways, consistent with the material's defect-mediated luminescence mechanism. This result, combined with a high relative PLQY (~67%) estimated under comparable conditions, underscores the robustness of $[(CH_3)NPh]_2MnBr_4$ against thermal quenching.

First-principles calculations

We performed DFT calculations using Vienna Ab initio simulation package (VASP)[36] with a plane wave basis set. We performed spin-polarized DFT calculations using the PBE exchange correlation (XC) functional[37] with Tkatchemko-Scheffler (TS) van der Waals corrections[38]

level of theory in conjunction with PAW plane wave basis sets of 500 eV energy cutoff in (1 x 1 x 1) k-point meshes for all systems. Geometry relaxation and electronic self-consistent loop were converged until the residual forces and energy differences were less than 0.02 eV/Å and 10^{-6} eV, respectively.

Data availability

The authors declare that the data supporting the findings of this study are available within this article and the Supplementary Information file. All raw data generated during the current study are also available from the corresponding author upon request. Crystallographic data for $[Me_3NPh]_2MnBr_4$ have been deposited at the Cambridge Crystallographic Data Centre, under deposition nos. CCDC 1896737. The input and output data files associated with the theoretical part of this study and all analysis can be found on GitHub at https://github.com/myung-group/Data_MnBrNCH.

References

1. Hu, D., Yao, L., Yang, B. & Ma, Y. Reverse intersystem crossing from upper triplet levels to excited singlet: A 'hot excition' path for organic light-emitting diodes. *Philosophical Transactions of the Royal Society A: Mathematical, Physical and Engineering Sciences* **373**, (2015).
2. Stranks, S. D. & Snaith, H. J. Metal-halide perovskites for photovoltaic and light-emitting devices. *Nature Nanotechnology* **10**, 391–402 (2015).
3. Kovalenko, M. V., Protesescu, L. & Bodnarchuk, M. I. Properties and potential optoelectronic applications of lead halide perovskite nanocrystals. *Science* **358**, 745–750 (2017).
4. Sutherland, B. R. & Sargent, E. H. Perovskite photonic sources. *Nature Photonics* **10**, 295–302 (2016).
5. Xing, G. *et al.* Low-temperature solution-processed wavelength-tunable perovskites for lasing. *Nature Materials* **13**, 476–480 (2014).
6. Zhao, F., Song, Z., Zhao, J. & Liu, Q. Double perovskite Cs2AgInCl6:Cr3+: Broadband and near-infrared luminescent materials. *Inorganic Chemistry Frontiers* **6**, 3621–3628 (2019).

7. Zelewski, S. J. *et al.* Revealing the nature of photoluminescence emission in the metal-halide double perovskite Cs2AgBiBr6. *Journal of Materials Chemistry C* **7**, 8350–8356 (2019).

8. Baldo, M. A. & Forrest, S. R. Highly efficient phosphorescent emission from organic electroluminescent devices. *Nature* **395**, 151–154 (1998).

9. Chihaya Adachi, Marc A. Baldo, Mark E. Thompson, and S. R. F. Nearly 100% internal phosphorescence efficiency in an organic light-emitting device. *Journal of Applied Physics* **90**, 5048–5051 (2001).

10. Jianzhang Zhao, S. J. and H. G. Triplet–triplet annihilation based upconversion- from triplet sensitizers and triplet acceptors to upconversion quantum yields. *RSC Advances* **1**, 937–950 (2011).

11. Jana, A., Myung, C. W., Sree, V. G. & Kim, K. S. Upconversion and multiexciton generation in organic Mn(ii) complex boost the quantum yield to > 100%. *Materials Chemistry Frontiers* **6**, 3102–3114 (2022).

12. Yuen Yap Cheng, Burkhard Fuckel, Rowan W. MacQueen, Tony Khoury, Raphael G. C. R. Clady, Tim F. Schulze, N. J. Ekins-Daukes, Maxwell J. Crossley, Bernd Stannowski, K. L. and T. W. S. Environmental Science Improving the light-harvesting of amorphous silicon solar cells with photochemical upconversion. *Energy & Environmental Science* **5**, 6953–6959 (2012).

13. Wu, B. *et al.* Indirect tail states formation by thermal-induced polar fluctuations in halide perovskites. *Nature Communications* **10**, 484 (2019).

14. Vandewal, K. *et al.* Efficient charge generation by relaxed charge-transfer states at organic interfaces Koen. *Nature Materials* **13**, 63–68 (2014).

15. Wright, A. D. *et al.* Electron-phonon coupling in hybrid lead halide perovskites. *Nature Communications* vol. 7 11755 (2016).

16. Herz, L. M. Charge-Carrier Dynamics in Organic-Inorganic Metal Halide Perovskites. *Annual Review of Physical Chemistry* **67**, 65–89 (2016).

17. Dar, M. I. *et al.* Origin of unusual bandgap shift and dual emission in organic-inorganic lead halide perovskites. *Science Advances* **2**, e1601156 (2016).

18. Sutter-Fella, C. M. *et al.* High Photoluminescence Quantum Yield in Band Gap Tunable Bromide Containing Mixed Halide Perovskites. *Nano Letters* **16**, 800–806 (2016).

19. T. Schmidt, K. Lischka, W. Z. Excitation-power dependence ofthe near-band-edge photoluminescence of semiconductors. *Physical Review B - Condensed Matter and Materials Physics* **45**, 8989–8994 (1992).

20. Adrián Francisco-López, Bethan Charles, Oliver J. Weber, M. Isabel Alonso, Miquel Garriga, Mariano Campoy-Quiles, Mark T. Weller, and A. R. G. Equal Footing of Thermal Expansion and Electron−Phonon Interaction in the Temperature Dependence of Lead HalidePerovskite Band Gaps. *The Journal of Physical Chemistry Letters* **10**, 2971–2977 (2019).

21. Dohner, E. R., Ja, A., Bradshaw, L. R. & Karunadasa, H. I. Intrinsic White-Light

Emission from Layered Hybrid Perovskites. *Journal of the American Chemical Society* **136**, 13154–13157 (2014).

22. Yangui, A. *et al.* Structural phase transition causing anomalous photoluminescence behavior in perovskite (C6H11NH3)2[PbI4]. *The Journal of Chemical Physics* **143**, 224201 (2015).

23. Booker, E. P. *et al.* Formation of Long-Lived Color Centers for Broadband Visible Light Emission in Low-Dimensional Layered Perovskites. *Journal of the American Chemical Society* **139**, 18632–18639 (2017).

24. Yu, J. *et al.* Broadband Extrinsic Self-Trapped Exciton Emission in Sn-Doped 2D Lead-Halide Perovskites. *Advanced Materials* **31**, 1806385 (2019).

25. Gaponenko, M. S. *et al.* Temperature-dependent photoluminescence of PbS quantum dots in glass: Evidence of exciton state splitting and carrier trapping. *Physical Reverw B* **82**, 125320 (2010).

26. Eline M. Hutter, María C. Gélvez-Rueda, Anna Osherov, Vladimir Bulović, Ferdinand C. Grozema, Samuel D. Stranks Savenije, and T. J. S. Direct–indirect character of the bandgap inmethylammounium lead iodide perovskite. *Nature Materials* **16**, 115–121 (2016).

27. Ball, J. M. & Petrozza, A. Defects in perovskite-halides and their effects in solar cells. *Nature Energy* **1**, 16149 (2016).

28. Rinku Saran, Amelie Heuer-Jungemann, Antonios G. Kanaras, and R. J. C. Giant Bandgap Renormalization and Exciton–PhononScattering in Perovskite Nanocrystals. *Advanced Optical Materials* **5**, 1700231 (2017).

29. R. Seguin, S. Rodt, A. Strittmatter, L. Reißmann, T. Bartel, A. Hoffmann, D. Bimberg, E. H. and D. G. Multi-excitonic complexes in single InGaN quantum dots. *Applied Physics Letters* **84**, 4023–4025 (2004).

30. Johnson Lee, Emil S. Koteles, and M. O. V. Luminescence linewidths of excitons in GaAs quantum wells below 150 K. *Physical Review B - Condensed Matter and Materials Physics* **33**, 5512–5516 (1986).

31. Felix Deschler, Michael Price, Sandeep Pathak, Lina E. Klintberg, David-Dominik Jarausch, Ruben Higler, Sven Hüttner, Tomas Leijtens, Samuel D. Stranks, Henry J. Snaith, Mete Atatüre, Richard T. Phillips, and R. H. F. High Photoluminescence Efficiency and Optically Pumped Lasing inSolution-Processed Mixed Halide Perovskite Semiconductors. *The Journal of Physical Chemistry Letters* **5**, 1421–1426 (2014).

32. Peán, E. V., Dimitrov, S., De Castro, C. S. & Davies, M. L. Interpreting time-resolved photoluminescence of perovskite materials. *Physical Chemistry Chemical Physics* **22**, 28345–28358 (2020).

33. Liu, Y. *et al.* Temperature-dependent photoluminescence spectra and decay dynamics of MAPbBr3 and MAPbI3 thin films. *AIP Advances* **8**, 095108 (2018).

34. He, H. *et al.* Exciton localization in solution-processed organolead trihalide perovskites. *Nature Communications* **7**, 10896 (2016).

35. Tarekegne, A. T. *et al.* Impacts of carrier capture processes in the thermal quenching of photoluminescence in Al–N co-doped SiC. *Applied Physics B: Lasers and Optics* **125**, 172 (2019).

36. G. Kresse, J. F. Efficient iterative schemes for ab initio total-energy calculations using a plane-wave basis set. *Physical Review B - Condensed Matter and Materials Physics* **54**, 11169 (1996).

37. Perdew, J. P., Burke, K. & Ernzerhof, M. Generalized gradient approximation made simple. *Physical Review Letters* **77**, 3865–3868 (1996).

38. Tkatchenko, A. & Scheffler, M. Accurate molecular van der Waals interactions from ground-state electron density and free-atom reference data. *Physical Review Letters* **102**, 073005 (2009).

39. Mannodi-Kanakkithodi, A., Park, J. S., Martinson, A. B. F. & Chan, M. K. Y. Defect Energetics in Pseudo-Cubic Mixed Halide Lead Perovskites from First-Principles. *Journal of Physical Chemistry C* **124**, 16729–16738 (2020).

Acknowledgements

This work was supported from the National Research Foundation of Korea (NRF) grant funded by the Korea government (MSIT) (2021R1A2C1006113 & RS-2022-NR072058) and Institute for Basic Science (IBS-R036-D1). C.W.M and W.W.C are grateful for the computational support from the Korea Institute of Science and Technology Information (KISTI) for the Nurion cluster (KSC-2022-CRE-0113, KSC-2022-CRE-0469, KSC-2023-CRE-0050, KSC-2023-CRE-0059, KSC-2023-CRE-0261, KSC-2023-CRE-0472, KSC-2024-CRE-0509, KSC-2024-CRE-0359, KSC-2024-CRE-0358, KSC-2024-CRE-0088, KSC-2024-CRE-0117). Computational work for this research was partially performed on the Olaf supercomputer supported by IBS Research Solution Center and on the GPU cluster supported by NIPA.

Author contributions

Competing interests

The authors declare no competing interests.

Additional information

Supplementary information The online version contains

supplementary material available at ooooo.

Correspondence and requests for materials should be addressed to R. T. Y.P.

Supporting information on

Temperature-independent emission in a $[(CH_3)NPh]_2MnBr_4$ single crystal analogous to thermally activated delayed fluorescence

Mutibah Alanazi[1], Atanu Jana[2], Won Woong Choi[3,4], Robert A. Taylor[1], Chang Woo Myung[3,4], Youngsin Park[5]

[1]Clarendon Laboratory, Department of Physics, University of Oxford, Parks Road, Oxford OX1 3PU, UK

[2]Division of Physics and Semiconductor, Dongguk University, Seoul 04620, Korea

[3]Department of Energy Science, Sungkyunkwan University, Suwon 16419, Korea

[4]Center for 2D Quantum Heterostructures, Institute for Basic Science (IBS), Suwon 16419, Korea

[5]Department of Chemistry, College of Natural Science, Ulsan National Institute of Science and Technology, Ulsan 44919, Korea

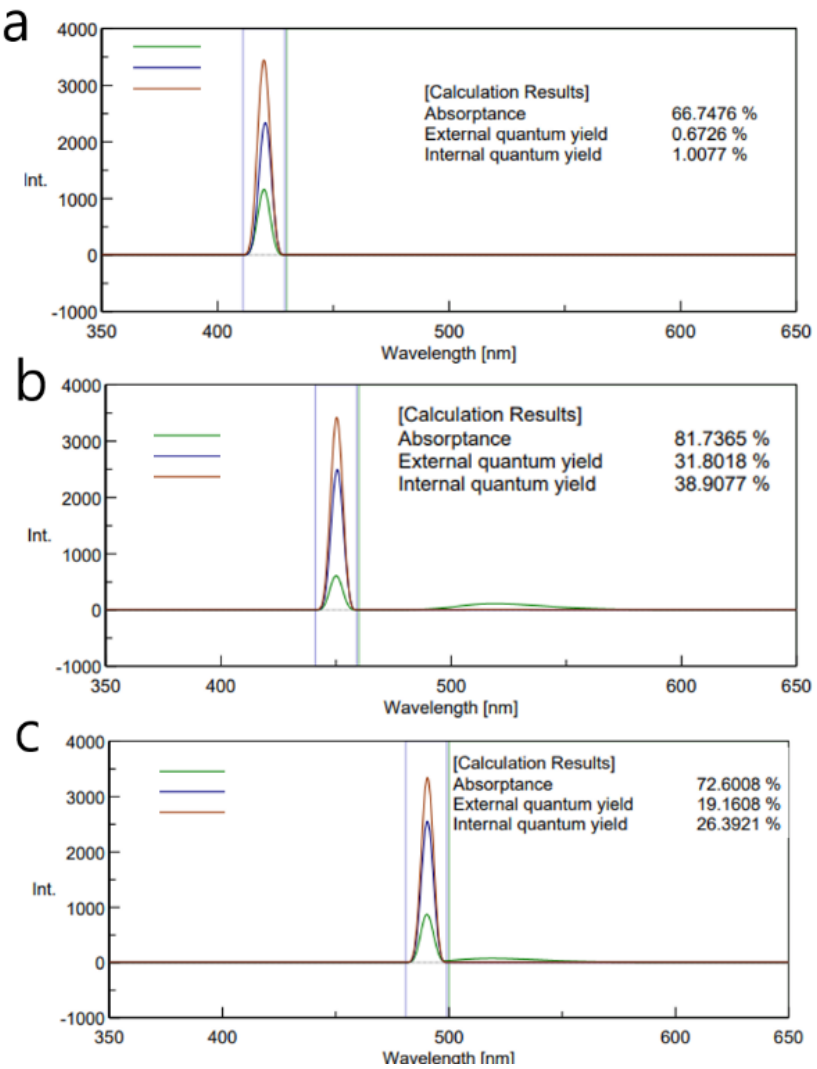

Fig. S1. AQY measurements at different excitation wavelengths. (a) 410 nm (b) 450 nm, and (c) 490 nm. Quantum yield [%] = $S_2/(S_0-S_1)$ ×100. S_1 = area scattered from the sample, S_2 = area emitted from sample, S_0 = area from incident light. S_0 was measured with nothing in the sample holder. The solid colors are direct (green), indirect (red), and reference (blue) measurements.

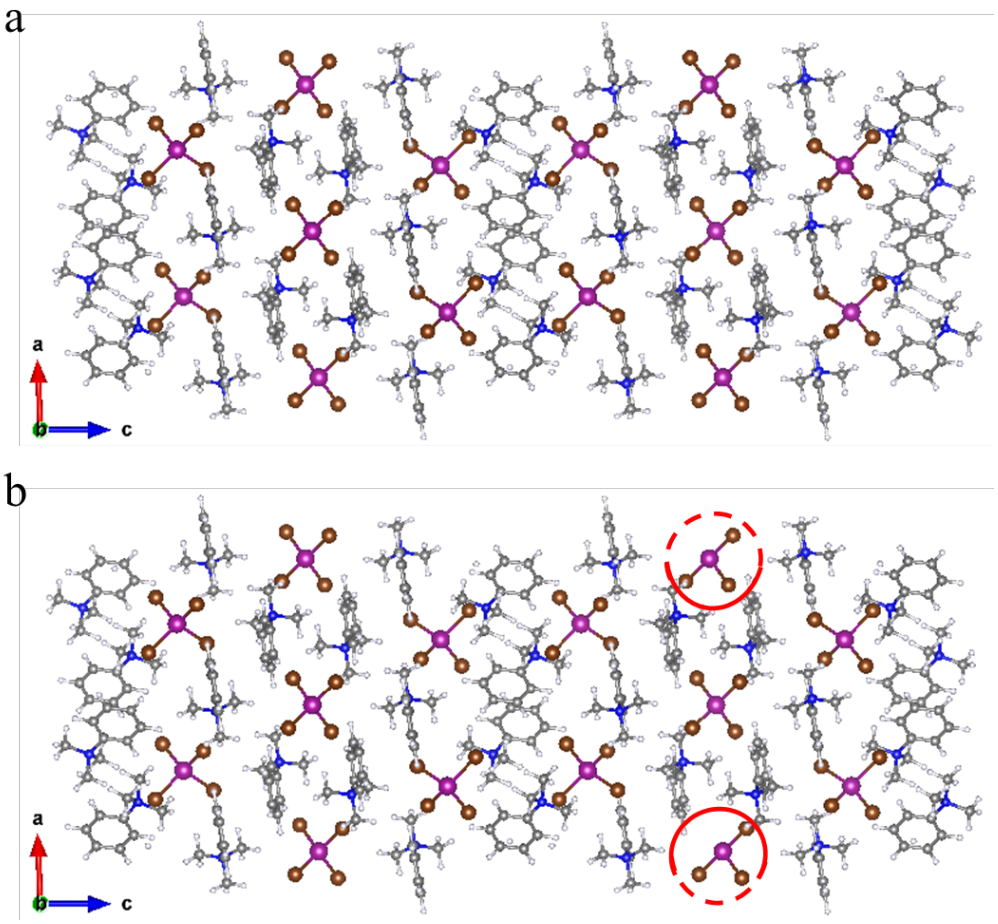

Fig. S2. Structures of (a) single-crystal $[Me_3NPh]_2MnBr_4$ and (b) the defect system, where one Br atom is removed from $[Me_3NPh]_2MnBr_4$. The defect caused by Br removal is highlighted with a red circle. (Mn – purple, Br – brown, N – blue, C – gray, H – white).

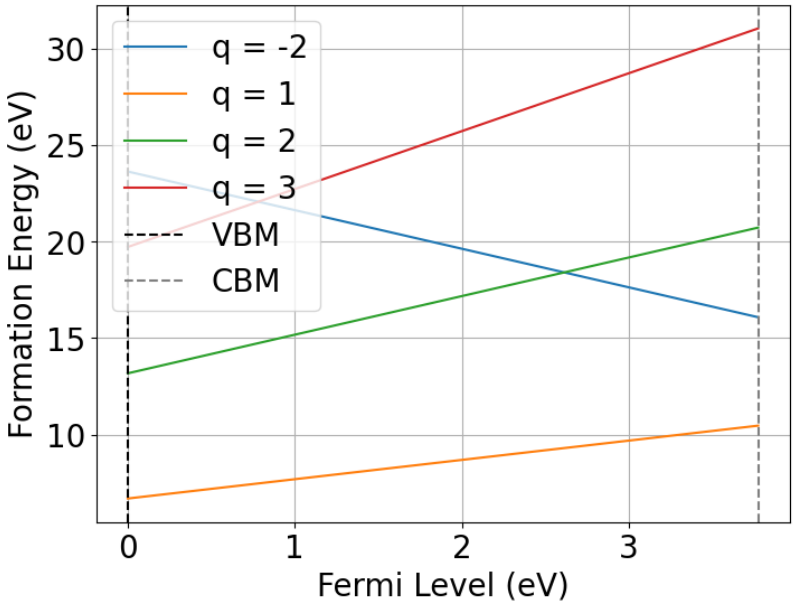

Fig. S3. Formation energies of the various vacancy defects, including single Mn vacancy (q = -2), single Br vacancy (q = 1), double Br vacancy (q = 2), and triple Br vacancy (q = 3).

We calculate the defect formation energy[39] with this equation:

$$E_{form} = E_{sys} - E_{bulk} - \sum n_i \mu_i + q(E_F + E_{corr})$$

E_{sys} is the total DFT energy of the defect containing supercell in a charge state q, E_{bulk} is the total DFT energy of the bulk supercell, n_i is the number of atoms which causing the vacancy defect, μ_i is the chemical potential of the relevant species involved in creating the defect, the fermi level E_F is the electron chemical potential referenced to the VBM of bulk system, and E_{corr} is the correction energy term. In here E_{corr} is 0. We calculate the chemical potential of Br atom from the gas phase, and Mn atom from the α-Mn solid phase. The formation energy of the vacancy defect is lowest at q = 1, indicating that the system with the removal of a single Br atom is the most favorable vacancy defect.

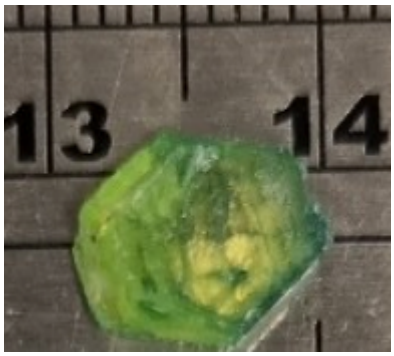

Fig. S4. Optical image of a $[(CH_3)NPh]_2MnBr_4$ single crystal. The crystal exhibits a distinct green coloration. The scale bar indicates millimeter measurements, highlighting the size of the crystal.

An optical image of a $[(CH_3)NPh]_2MnBr_4$ single crystal is presented. The crystal, with its characteristic green hue, demonstrates a well-defined hexagonal shape. The scale in the background provides a size reference in millimeters, indicating the crystal's dimensions. This image supports the high-quality crystallinity and morphology of the synthesized $[(CH_3)NPh]_2MnBr_4$ crystals used in the study.

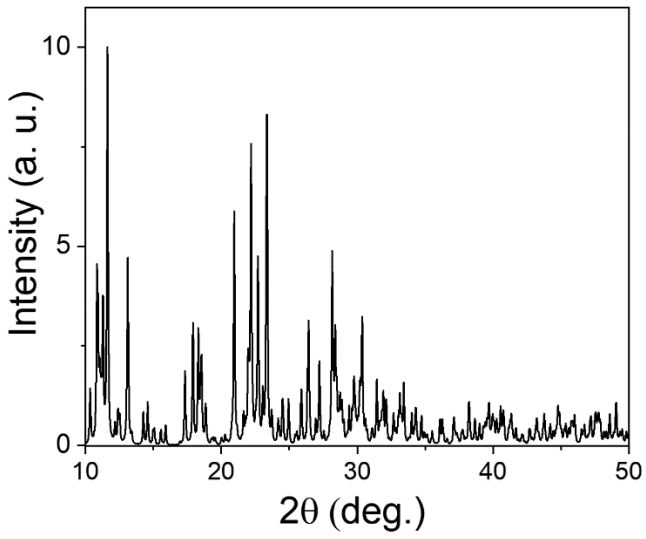

Fig. S5. Powder X-ray diffraction (XRD) pattern of $[(CH_3)NPh]_2MnBr_4$ single crystal measured at 223 K.

The powder XRD pattern of $[(CH_3)NPh]_2MnBr4$ single crystal exhibits sharp and well-defined diffraction peaks, indicating high crystallinity and phase purity of the synthesized material. The pattern shows multiple intense peaks in the 2θ range of 10° to 50°, with prominent reflections observed at lower angles (10°-30°). The high intensity and narrow width of the diffraction peaks further confirm the high quality and long-range order of the crystal structure, supporting the observed optical properties and carrier dynamics discussed in the main text.

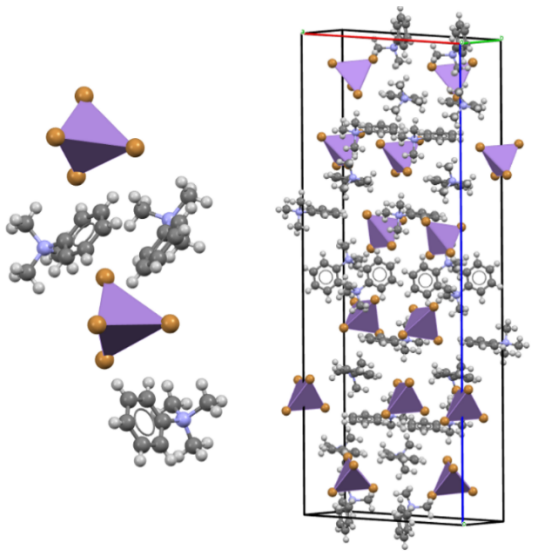

Fig. **S6.** Crystal structure of $[(CH_3)NPh]_2MnBr_4$ single crystal obtained from XRD measurements. The structure is shown with different colors representing specific atoms: manganese (Mn) in purple, bromine (Br) in orange, carbon (C) in gray, nitrogen (N) in blue, and hydrogen (H) in white. The organic cation $[(CH_3)NPh]$ is depicted with carbon (C) atoms in gray, nitrogen (N) atoms in blue, and hydrogen (H) atoms in white. The right side of the figure shows the unit cell, illustrating the arrangement of $MnBr_4$ tetrahedra and organic cations within the crystal lattice.

Interestingly, our temperature-dependent XRD analysis (Table S1) reveals only minimal changes in lattice constants across the studied temperature range. This structural stability is remarkable and provides crucial insights into the material's optoelectronic properties. Despite the lack of significant structural changes, we observe notable variations in the optical

characteristics, particularly in PL intensity and decay dynamics. This apparent discrepancy between structural stability and varying optical properties suggests that the observed temperature-dependent phenomena are primarily driven by subtle electronic and vibrational changes rather than large-scale structural modifications. Several factors may contribute to this behavior:

Table S1. Crystallographic data and structural refinement parameters for $[(CH_3)NPh]_2MnBr_4$ single crystal at different temperatures.

Temperature (K)	Space group	a (Å)	b (Å)	C (Å)	Volume
223	C 2/c	17.1030(8) α = 90°	9.2048(4) β =92.670(2)	47.038(2) γ = 90°	7397.1(6)
293	C 2/c	17.1271(9) α = 90°.	9.1787(5) β = 92.605(2)°	47.166(3) γ = 90°	7407.1(7)

Table S1 shows temperature-dependent unit cell parameters, space group, and refined structural details of $[(CH_3)NPh]_2MnBr_4$ single crystal as determined by single crystal X-ray diffraction. Data is presented for temperatures of 223 K and 293 K, showcasing the structural stability of the material across this temperature range.